



Cite this: DOI: 10.1039/d6sc01575a

All publication charges for this article have been paid for by the Royal Society of Chemistry

## ZrO<sub>2</sub>-induced d–d spatial coordination effects of Ru single-atom catalysts to boost the oxygen evolution reaction

Dandan Yu,<sup>a</sup> Bin Liu,<sup>a</sup> Dongming Li,<sup>a</sup> Junkai Yu,<sup>a</sup> Xijie Lan,<sup>a</sup> Shuhong Liu,<sup>a</sup> Zhuxin Li,<sup>b</sup> Pengyun Gao,<sup>b</sup> Yong Zhang<sup>\*a</sup> and Hong Zhao<sup>†b</sup>

Proton exchange membrane water electrolysis (PEMWE) is a leading strategy for producing green hydrogen from intermittent renewable energy. However, the high anodic energy barrier of the oxygen evolution reaction (OER), in a strongly acidic and highly oxidative operating environment, poses severe challenges for catalyst design. Herein, based on a unique d–d spatial coordination design, tetragonal zirconia-supported Ru single-atom catalysts (Ru-RSZ) were synthesized, which exhibited an overpotential as low as 208 mV and a mass activity of 1452.61 A g<sub>Ru</sub><sup>-1</sup> @ 1.51 V. Remarkably, these catalysts were stably operated for 500 h. X-ray absorption spectroscopy (XAS) and high-angle annular dark-field (HAADF) imaging demonstrated that Ru is atomically dispersed at Zr lattice sites in ZrO<sub>2</sub>, and the point-group symmetry of the Ru atom changes from *D*<sub>2h</sub> in RuO<sub>2</sub> to *D*<sub>2d</sub>. Density functional theory (DFT) calculations elucidated that the d-band center of Ru atoms was lowered by d–d spatial coordination effects, which weakened the strong adsorption of oxygen at Ru sites, eventually reducing the activation barrier of the OER rate-determining step. This work paves a new avenue to design high-efficiency and stable catalysts for hydrogen production.

Received 24th February 2026  
Accepted 7th April 2026

DOI: 10.1039/d6sc01575a

rsc.li/chemical-science

## Introduction

Against the backdrop of advancing green, low-carbon development and the global energy transition, hydrogen production from water electrolysis has emerged as a cornerstone technology for building the future energy system.<sup>1–4</sup> Proton exchange membrane water electrolysis (PEMWE) has garnered significant attention due to its higher current density, rapid kinetics and higher stack efficiency (70–77%) in contrast to alkaline water electrolysis.<sup>5,6</sup> However, the oxygen evolution reaction (OER) of PEMWE systems involves complex multi-step proton-coupled electron transfer processes and demonstrates sluggish kinetics, which significantly limit the overall efficiency of water electrolysis.<sup>7,8</sup> Furthermore, protonation and solvation effects in acidic media pose substantial challenges to the stability of anode catalysts.<sup>9</sup> Currently, only iridium-based oxides are widely used as OER catalysts, but the disadvantages of high-cost and scarcity severely limit their large-scale applications.<sup>10,11</sup> To address these challenges, extensive research has focused on finding alternative catalysts, with cost-effective (10 times cheaper than iridium)<sup>12</sup> and Earth-abundant<sup>13</sup> ruthenium (Ru) emerging as a promising iridium substitute owing to its

comparable catalytic activity.<sup>14–16</sup> Nevertheless, the durability of ruthenium oxides remains limited and insufficient to meet the long-term operational requirements of commercial-scale PEMWE systems.<sup>17</sup> Moreover, as a noble metal, ruthenium still entails substantial cost.<sup>18</sup> To satisfy the commercial demands of PEMWE for industrial hydrogen production, it is imperative to develop low-cost Ru electrocatalysts with high activity and long-term stability.

Nowadays, the development of Ru-based electrocatalysts primarily encompasses doping and defect engineering, interface engineering, hybridized orbital engineering, *etc.*<sup>16,19,20</sup> Among these, orbital coupling between RuO<sub>2</sub> and heteroatom dopants has demonstrated pronounced enhancement and stabilization of active sites.<sup>21</sup> For example, Pb doping produces Pb–O–Ru 6s–2p–4d orbital hybridization that increases the energy required to remove lattice oxygen, thereby suppressing excessive oxidation of Ru.<sup>22</sup> Similarly, unique lanthanide dopants induce f–p–d gradient orbital coupling that can modify adsorption energies of reaction intermediates and inhibit involvement of lattice oxygen, thus preventing over-oxidation of Ru.<sup>23</sup> However, Ru–M orbital coupling mediated by O bridges is weakened by the presence of O 2p orbitals. Moreover, studies of dopant-induced orbital coupling based on the rutile structure have frequently neglected the strong influence of local atomic coordination, although some studies have compared the OER performance of Ru located at sites of different symmetries in other structures such as pyrochlore<sup>24</sup> and perovskites.<sup>25,26</sup>

<sup>a</sup>School of Materials Science and Engineering, Dalian Jiaotong University, Dalian, 116028, China. E-mail: zhangyong0411@126.com

<sup>b</sup>College of Material Science and Engineering, Sichuan University of Science and Engineering, Zigong, 643000, China. E-mail: zhaohong@suse.edu.cn



Investigations specifically addressing how crystal-structure-driven differences alter orbital coupling remain scarce. More importantly, substantial amounts of Ru catalysts are still required in doped RuO<sub>2</sub> systems, which does not satisfy the low-cost requirement of industrial hydrogen production.

In this work, an acid-resistant oxide, ZrO<sub>2</sub>, was adopted as the support to provide Ru atoms with a distinctive atomic coordination geometry (*P4<sub>2</sub>/nmc*).<sup>27</sup> A Ru single-atom catalyst supported on ZrO<sub>2</sub> (Ru-RSZ) was synthesized *via* a hydrothermal method. X-ray diffraction (XRD) and Raman characterization indicate that introduction of Ru stabilizes the tetragonal phase of ZrO<sub>2</sub>. Further high-angle annular dark-field scanning transmission electron microscopy (HAADF-STEM) and X-ray absorption spectroscopy (XAS) analyses reveal that Ru occupies Zr lattice sites, with site symmetry transformed from *D<sub>2h</sub>* in RuO<sub>2</sub> to *D<sub>2d</sub>* in ZrO<sub>2</sub>. Density functional theory (DFT) calculations reveal that the unique d–d interactions in Ru-RSZ furnish direct bonding, substantially lowering the Ru 4d-band center, suppressing strong adsorption of oxygen intermediates on Ru, reducing reaction barriers, and concurrently weakening Ru–O covalency to inhibit participation of lattice oxygen, thereby enhancing structural stability. The synthesized Ru-RSZ catalyst exhibits an overpotential reduced to 208 mV at a Ru loading of only 43.9 μg<sub>Ru</sub> cm<sup>−2</sup>, and chronopotentiometry at a current density of 10 mA cm<sup>−2</sup> shows that the catalyst remains stable for 500 h. Moreover, oxygen vacancies present in Ru-RSZ further reinforce the d–d interactions of Ru–Zr, contributing to the catalyst's activity and stability. This work provides an effective strategy for developing high-efficiency and low-cost electrocatalysts for industrial hydrogen production.

## Results and discussion

### Material design and theoretical calculation

To validate the feasibility of the design strategy, DFT calculations were conducted to systematically compare the electronic structure and stability of the ZrO<sub>2</sub>-supported Ru catalyst (denoted as Ru-RSZ) and commercial RuO<sub>2</sub> (Fig. 1a). Quantitative analysis of the intermetallic interactions provides direct evidence for the support stabilization effect: the integrated crystal orbital Hamilton population (ICOHP) for the Ru–Zr pair in Ru-RSZ is −0.001 eV, indicating a weak net bonding interaction.<sup>15</sup> In contrast, the ICOHP for the Ru–Ru pair in RuO<sub>2</sub> is +0.048 eV revealing a net antibonding interaction. Similarly, when Zr occupies the Ru sites in RuO<sub>2</sub> with *D<sub>2h</sub>* symmetry, a net antibonding interaction (ICOHP = +0.021 eV) is also observed (Fig. S1). The direct d–d interaction between Zr and Ru not only reinforces the lattice framework but also markedly alters the 4d orbital distribution at Ru sites (Fig. 1b). Projected density of states (PDOS) and electronic band structure analyses (Fig. 1c and S2) reveal that the d-band center of the Ru 4d orbitals in Ru-RSZ shifts downward and farther from the Fermi level compared to that in com-RuO<sub>2</sub>.<sup>22</sup> This modulation in the electronic structure suggests a weakened adsorption strength for oxygen evolution reaction intermediates, which is anticipated to mitigate the catalytic activity limitation inherent to conventional RuO<sub>2</sub> caused by the over-binding of intermediates, thereby enhancing the intrinsic activity.<sup>28</sup> Furthermore, the altered coordination environment induces a further separation between the Ru 4d and O 2p bands, characterized by a downward shift of both band centers, resulting in an enlarged characteristic band gap ( $\epsilon_{d-p}$ ) of 2.91 eV for Ru-RSZ compared to

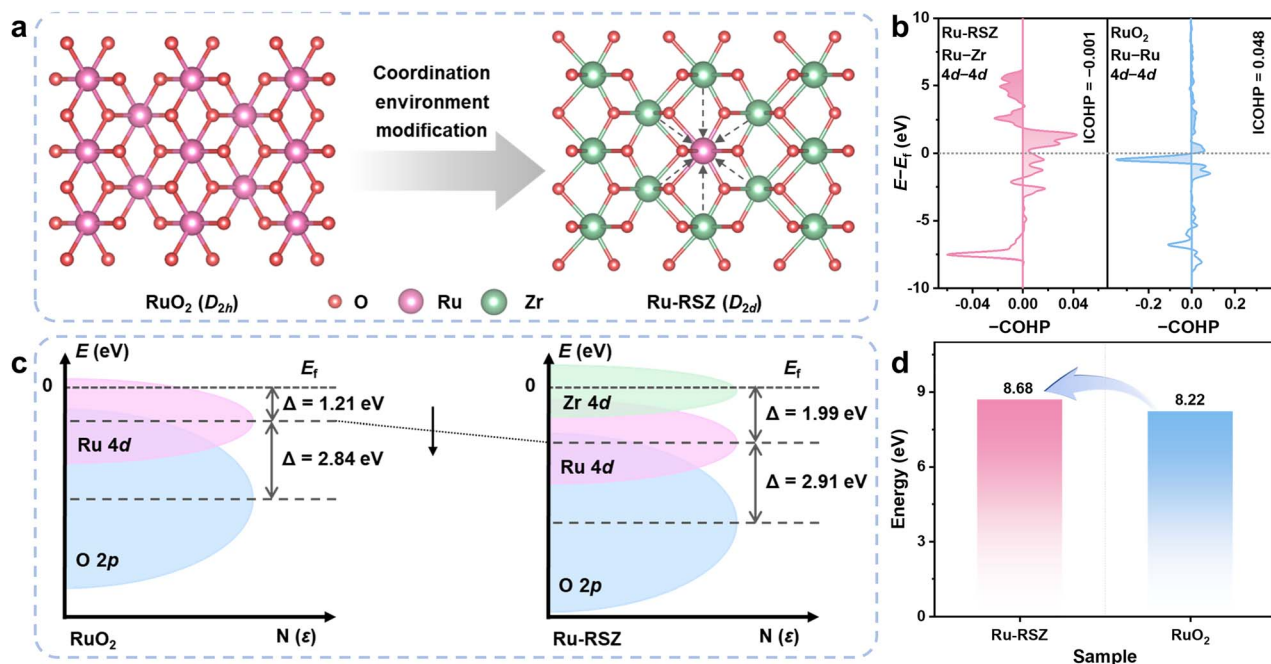


Fig. 1 (a) Schematic diagram of the design strategy for modifying the coordination environment of Ru. (b) Calculated COHP of Ru-RSZ and RuO<sub>2</sub>. (c) Schematic diagram of the band structure for Ru-RSZ and RuO<sub>2</sub>. (d) Ru vacancy formation energy of Ru-RSZ and RuO<sub>2</sub>.



2.84 eV for RuO<sub>2</sub>. This enlarged band gap indicates a reduced degree of covalent hybridization in the Ru–O bonds within Ru-RSZ, an electronic feature that contributes to suppressing the over-oxidation and dissolution of ruthenium under operational conditions, thereby enhancing the electrochemical stability of the catalyst.<sup>29</sup> The obviously increased Ru vacancy formation energy (Fig. 1d) in Ru-RSZ further corroborates, from a thermodynamic perspective, the superior stabilization effect exerted by the ZrO<sub>2</sub> support on the ruthenium active sites.<sup>20,30</sup>

### Material characterization and the coordination environment

Ru-RSZ was synthesized *via* the co-precipitation method (Fig. S3). The resulting precipitate was then subjected to hydrothermal treatment at 200 °C for 12 hours, followed by centrifugation and drying to obtain Ru-RSZ powder. The XRD

pattern confirms the presence of a tetragonal ZrO<sub>2</sub> phase (JCPDS 01-070-7300) in Ru-RSZ (Fig. 2a). No detectable peaks corresponding to Ru were observed, indicating that the lattice structure of ZrO<sub>2</sub> remains intact after Ru introduction (Fig. S4).<sup>31</sup> Notably, the XRD pattern of Ru-RSZ shifts slightly to higher diffraction angles compared to that of ZrO<sub>2</sub> (Fig. S5), indicating a decrease in the Ru-RSZ lattice constant owing to a smaller Ru atomic radius.<sup>32</sup> After the introduction of Ru, the peaks associated with the monoclinic phase of ZrO<sub>2</sub> were no longer detected, suggesting that Ru promotes the stabilization of the tetragonal phase. Raman spectroscopy (Fig. S6) confirmed the presence of the tetragonal ZrO<sub>2</sub> phase (t-ZrO<sub>2</sub>) in the Ru-RSZ sample, with characteristic peaks at 284, 457 and 645 cm<sup>-1</sup>.<sup>33,34</sup> No peaks from the monoclinic phase were observed. This result was in accordance with the above XRD

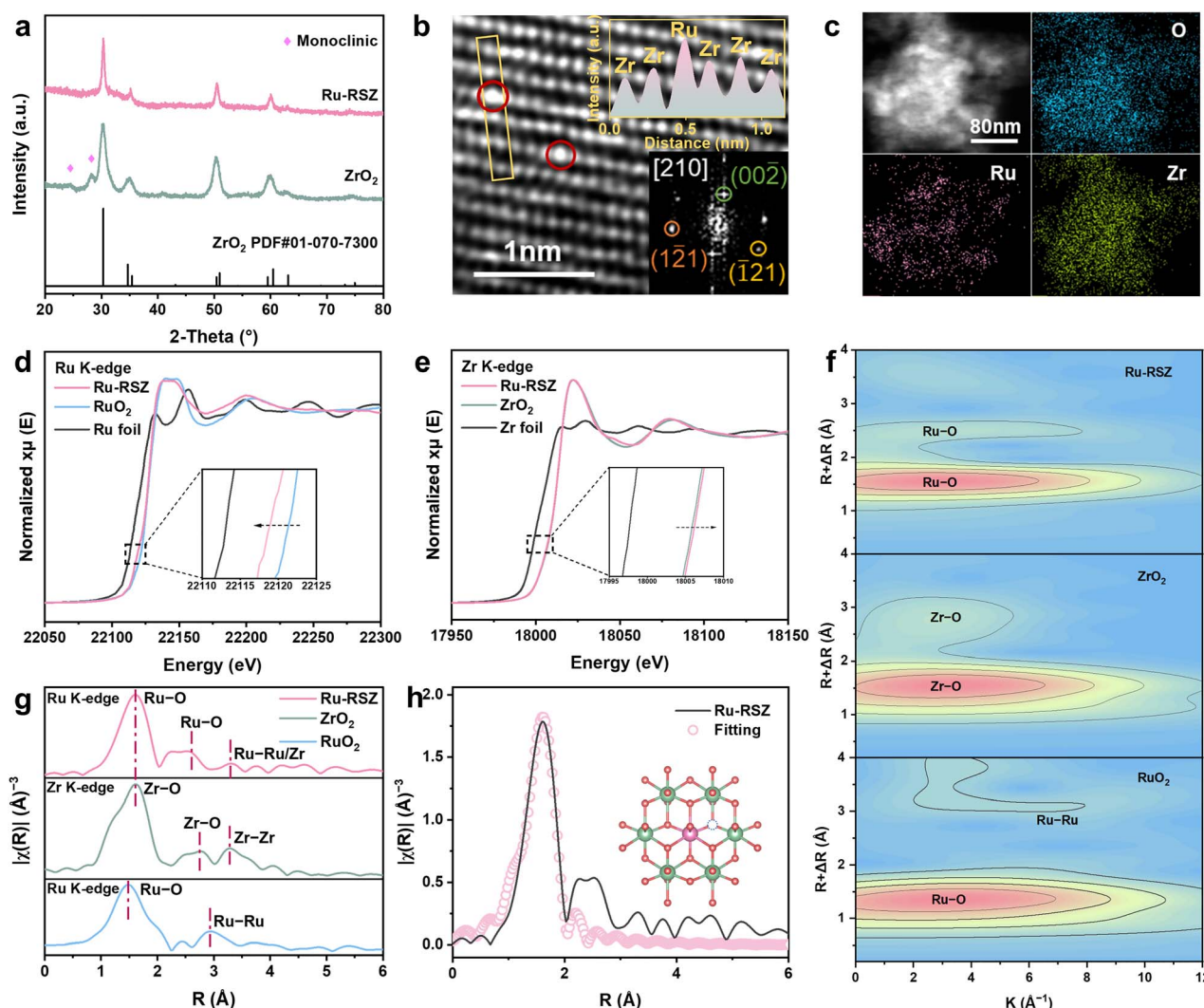


Fig. 2 (a) XRD patterns of Ru-RSZ and ZrO<sub>2</sub>. (b) HAADF-STEM and corresponding FFT image (inset) of Ru-RSZ along the [210] orientation with the Z-contrast intensity line profile extracted from the marked area. The bright spots highlighted by red circles correspond to isolated Ru atoms occupying Zr lattice sites. (c) HAADF-STEM image and corresponding EDS mapping of Ru-RSZ. (d) Normalized Ru K-edge XANES spectra of Ru-RSZ, RuO<sub>2</sub>, and Ru foil. (e) Normalized Zr K-edge XANES spectra of Ru-RSZ, ZrO<sub>2</sub> and Zr foil. (f) Wavelet-transformed  $k^3$ -weighted EXAFS signals of Ru-RSZ, ZrO<sub>2</sub> and RuO<sub>2</sub>. (g) Fourier transform  $R$ -space of the experimental EXAFS signal collected at the Ru K-edge for Ru-RSZ and RuO<sub>2</sub>, and the Zr K-edge for ZrO<sub>2</sub>. (h)  $R$ -Space fitting results of Ru K-edge XAFS spectra of Ru-RSZ.



results. Furthermore, two Raman bands corresponding to the tetragonal phase over the Ru-RSZ sample were blue-shifted, suggesting a strong metal-support interaction between Ru and ZrO<sub>2</sub>.<sup>35,36</sup>

To investigate the morphology and distribution of Ru atoms in Ru-RSZ, scanning electron microscopy (SEM) and spherical aberration-corrected HAADF-STEM imaging (Fig. 2b) were performed.<sup>37</sup> SEM and STEM images of Ru-RSZ reveal a morphology similar to that of ZrO<sub>2</sub>, with both materials consisting of nanoparticles approximately 8 nm in diameter (Fig. S7). The Z-contrast image acquired by HAADF-STEM (Fig. 2b), its Fast Fourier Transform (FFT) (inset) and the corresponding Z-contrast intensity profile show Ru (highlighted) randomly dispersed on Zr lattice sites in ZrO<sub>2</sub> projected along the [210] crystallographic direction. STEM-energy-dispersive spectroscopy (STEM-EDS) mapping (Fig. 2c, S8 and Table S1) indicates uniform distribution of Ru, Zr, and O in Ru-RSZ with no obvious segregation (Ru atom percentage of metallic elements in Ru-RSZ is ≈ 10.8 at%).

The electronic structure of Ru-RSZ was further characterized by using X-ray photoelectron spectroscopy (XPS) and XAS. The full XPS spectra of Ru-RSZ, RuO<sub>2</sub> and ZrO<sub>2</sub> are presented in Fig. S9. X-ray absorption near-edge spectroscopy (XANES) of the Ru K-edge reveals a shift of the absorption edge to lower energy in Ru-RSZ compared to RuO<sub>2</sub>, suggesting a decrease in the Ru valence state (Fig. 2d). The Zr K-edge XANES spectra indicate a near-edge absorption energy slightly higher than that of ZrO<sub>2</sub> (Fig. 2e). The Zr 3d XPS spectrum (Fig. S10) of Ru-RSZ exhibits a discernible binding energy upshift of approximately 0.14 eV and 0.2 eV for the Zr 3d<sub>5/2</sub> and Zr 3d<sub>3/2</sub> peaks, respectively, compared to ZrO<sub>2</sub>, suggesting a relatively higher oxidation state of Zr in Ru-RSZ, which agrees well with the XANES analysis results.<sup>38,39</sup> Meanwhile, the deconvolution of the Ru 3p XPS spectrum (Fig. S11 and Table S2) indicates that the proportion of Ru<sup>III</sup> in Ru-RSZ is 74%, significantly higher than that in RuO<sub>2</sub> (26%).<sup>40</sup> This higher ratio suggests electron transfer from the ZrO<sub>2</sub> support to Ru, leading to a reorganization of its local electronic structure, a conclusion further supported by the distinct negative shift in the Ru 3p binding energy peaks. The pre-reduction effect of Zr on Ru can effectively prevent the excessive oxidative dissolution of Ru during the OER process, thereby enhancing its stability.<sup>41</sup>

Wavelet Transform Extended X-ray Absorption Fine Structure (WT-EXAFS) indicates that the coordination environment of Ru in Ru-RSZ is the same as that of the Zr sites in ZrO<sub>2</sub> (featuring two Ru/Zr–O coordination bonds),<sup>20</sup> distinct from that in RuO<sub>2</sub> (which exhibits Ru–O and Ru–Ru coordination bonds) (Fig. 2f). Concurrently, Ru K-edge EXAFS reveals Ru–O and Ru–Ru/Zr scattering peaks in Ru-RSZ at approximately 1.6 Å, 2.8 Å, and 3.2 Å. Zr K-edge EXAFS likewise shows Zr–O and Zr–Zr scattering peaks in Ru-RSZ at 1.6 Å, 2.7 Å, and 3.2 Å, demonstrating that Ru and Zr occupy the same metal sites in the Ru/Zr oxide phase, with a symmetry change from D<sub>2h</sub> to D<sub>2d</sub> (Fig. 2g, S12 and S13). In addition, EXAFS fitting results (Fig. 2h and Table S3) indicate a Ru–O coordination number of 7.4 in Ru-RSZ, evidencing a significant presence of oxygen vacancies.<sup>16</sup> Furthermore, the O 1s peak (Fig. S14) of Ru-RSZ is deconvoluted

into three peaks at 529.6, 530.7, and 532.7 eV, corresponding to the lattice oxygen (O<sub>L</sub>), surface oxygen vacancies (O<sub>V</sub>) and surface oxygen adsorbates (O<sub>ads</sub>), respectively.<sup>42,43</sup> The peak fitting results of the O 1s XPS spectra (Table S4) indicate that the proportion of oxygen vacancies in Ru-RSZ is 43%, significantly higher than the 29% observed in ZrO<sub>2</sub>, suggesting a significant increase after Ru introduction. This finding is further corroborated by electron paramagnetic resonance (EPR) measurements (Fig. S15), which reveal a characteristic signal at *g* = 2.005 for Ru-RSZ (Fig. S15), corresponding to unpaired electrons trapped at oxygen vacancies, in good agreement with the XPS O 1s analysis.<sup>29</sup>

### Electrochemical performance in acidic electrolytes

The OER performance of Ru-RSZ, ZrO<sub>2</sub> and RuO<sub>2</sub> catalysts was evaluated in a three-electrode system using 0.5 M H<sub>2</sub>SO<sub>4</sub> as the electrolyte. Linear sweep voltammetry (LSV) and corresponding Tafel analysis (Fig. 3a and b) demonstrated that the Ru-RSZ catalyst exhibits outstanding electrocatalytic activity, requiring an overpotential ( $\eta$ ) of only 208 mV to achieve a current density of 10 mA cm<sup>-2</sup> along with a Tafel slope of 62.15 mV dec<sup>-1</sup>. These values are substantially lower than those of RuO<sub>2</sub> (265 mV and 71.97 mV dec<sup>-1</sup>, respectively), while the ZrO<sub>2</sub> support showed negligible OER activity. Notably, the Ru specific mass activity (Fig. 3c and S16) of the Ru-RSZ catalyst was calculated to be as high as 1452.61 A g<sub>Ru</sub><sup>-1</sup> at  $\eta$  = 1.51 V, which is more than 40.1 times higher than that of RuO<sub>2</sub> (36.21 A g<sub>Ru</sub><sup>-1</sup> at 1.51 V). To further evaluate the intrinsic activity of the Ru species, the turnover frequency (TOF) was calculated and plotted against the overpotential (Fig. S17). The calculated TOF value for Ru-RSZ reached 0.38 s<sup>-1</sup> at an overpotential of 1.51 V, representing a 38-fold enhancement over that of RuO<sub>2</sub> (0.01 s<sup>-1</sup>). Double-layer capacitance (*C*<sub>dl</sub>) was measured to determine the electrochemical active surface area (ECSA) for evaluating the OER performance (Fig. 3d, S18 and Table S5). Ru-RSZ demonstrates the highest *C*<sub>dl</sub> of 13.67 mF cm<sup>-2</sup> and ECSA (390.57 cm<sup>2</sup>), values approximately 1.43 times greater than those of RuO<sub>2</sub> (9.56 mF cm<sup>-2</sup> and 273.14 cm<sup>2</sup>, respectively). This indicates a significantly increased number of available active sites in Ru-RSZ, which effectively enhances its OER performance. Additionally, the OER activity normalized to the electrochemical surface area of Ru-RSZ and RuO<sub>2</sub> was also calculated (Fig. S19). The ECSA-normalized mass activity of Ru-RSZ reached 0.16 mA cm<sup>-2</sup> at 1.51 V (vs. RHE), which is 3.2 times higher than that of RuO<sub>2</sub> (0.05 mA cm<sup>-2</sup>), further demonstrating its superior intrinsic OER catalytic activity.

Electrochemical impedance spectroscopy (EIS) is a powerful technique to examine the electrical charge transfer behavior across interfaces and phases in electrochemical systems.<sup>44</sup> The EIS measurements (Fig. 3e) revealed well-defined semicircular Nyquist plots for Ru-RSZ, RuO<sub>2</sub>, and ZrO<sub>2</sub>.<sup>45</sup> Among these, Ru-RSZ exhibited a semicircle with a notably smaller radius compared to RuO<sub>2</sub> and ZrO<sub>2</sub>. The fitting results (Table S6) indicated a significantly lower charge-transfer resistance (*R*<sub>ct</sub>) and more efficient electron transfer across the electrode/electrolyte interface. The stability of Ru-RSZ was evaluated by



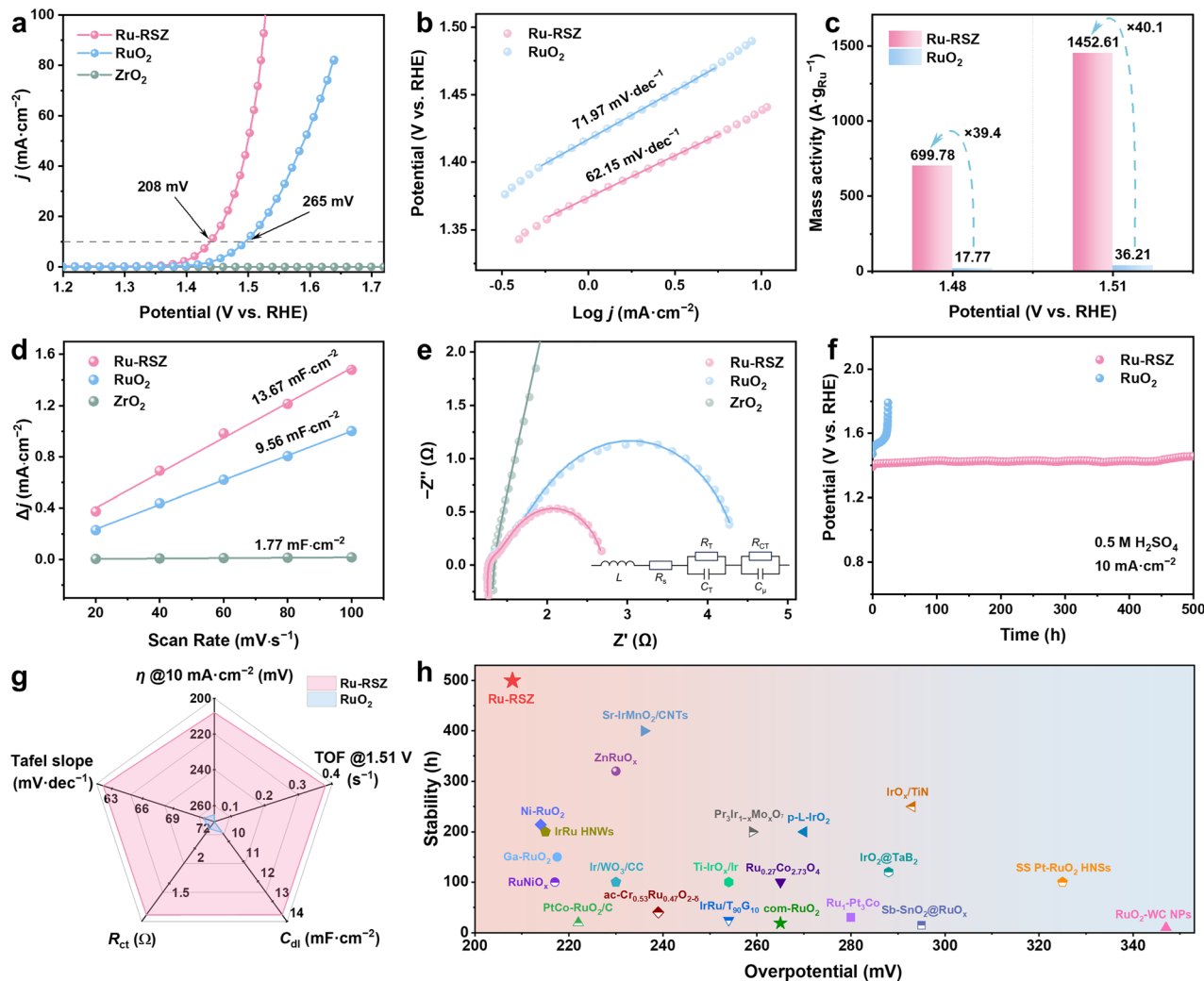


Fig. 3 Electrocatalytic OER performance evaluation in 0.5 M H<sub>2</sub>SO<sub>4</sub> electrolyte. (a) LSV polarization curves and (b) Tafel plots of Ru-RSZ and RuO<sub>2</sub>. (c) Ru mass activities of Ru-RSZ and RuO<sub>2</sub> at 1.48 and 1.51 V vs. RHE. (d) C<sub>dl</sub> plots and (e) Nyquist plots of Ru-RSZ, ZrO<sub>2</sub> and RuO<sub>2</sub> derived from CV curves. (f) Chronopotentiometry test at 10 mA cm<sup>-2</sup> of electrocatalysts. (g) Summary of some major OER performance metrics of Ru-RSZ and RuO<sub>2</sub>. (h) Comparison of the overpotential and stability of Ru-RSZ with previously reported OER electrocatalysts in acidic electrolyte.

chronopotentiometry (CP) at a constant current density of 10 mA cm<sup>-2</sup> (Fig. 3f). Compared to the commercial RuO<sub>2</sub> catalyst, Ru-RSZ exhibited excellent stability, retaining most of its potential over a 500-hour period, with some cases even showing a slight performance enhancement as indicated by a decrease in the overpotential. Post-reaction characterization (Fig. S20) confirmed that the crystal structure and atomic dispersion of Ru remained intact, further supporting the structural robustness of the catalyst. With regard to the OER, Ru-RSZ outperformed RuO<sub>2</sub> across all five considered dimensions (Fig. 3g and Table S7). The outstanding activity and stability of Ru-RSZ significantly exceed those of previously reported noble metal electrocatalysts in acidic electrolytes (Fig. 3h and Table S8).

### Insights into the OER catalytic mechanism

To elucidate the regulatory mechanism of oxygen vacancies on the electronic structure of catalytic sites, systematic DFT

calculations were conducted on Ru-RSZ-O<sub>v</sub>, Ru-RSZ, and RuO<sub>2</sub>. Structural optimization (Fig. 4a) reveals that the formation of an oxygen vacancy induces notable local structural relaxation, reducing the distance between Ru and the adjacent Zr atom from 3.98 Å (Ru-RSZ) to 2.87 Å (Ru-RSZ-O<sub>v</sub>), thereby creating favorable geometric conditions for interatomic orbital interactions.<sup>22</sup> Charge density difference and Bader charge analyses (Fig. 4b and Table S9) collectively unveil the charge redistribution triggered by the oxygen vacancies, with pronounced electron accumulation observed in the Ru-Zr bridging region, preliminarily indicating enhanced d-d orbital interaction.<sup>46</sup> The Bader charge on the Ru atom in Ru-RSZ-O<sub>v</sub> decreases to +0.3099|e|, lower than its value of +0.8249|e| in Ru-RSZ, while the charge on the adjacent Zr atom also decreases from +1.6345|e| to +1.5131|e|, suggesting weakened electron localization and enhanced covalency.<sup>47</sup> Notably, the Bader charge of Ru in Ru-RSZ-O<sub>v</sub> is lower than that of Ru in RuO<sub>2</sub> (+1.4893|e|), while the charge of its Zr is higher than that of Zr in ZrO<sub>2</sub>



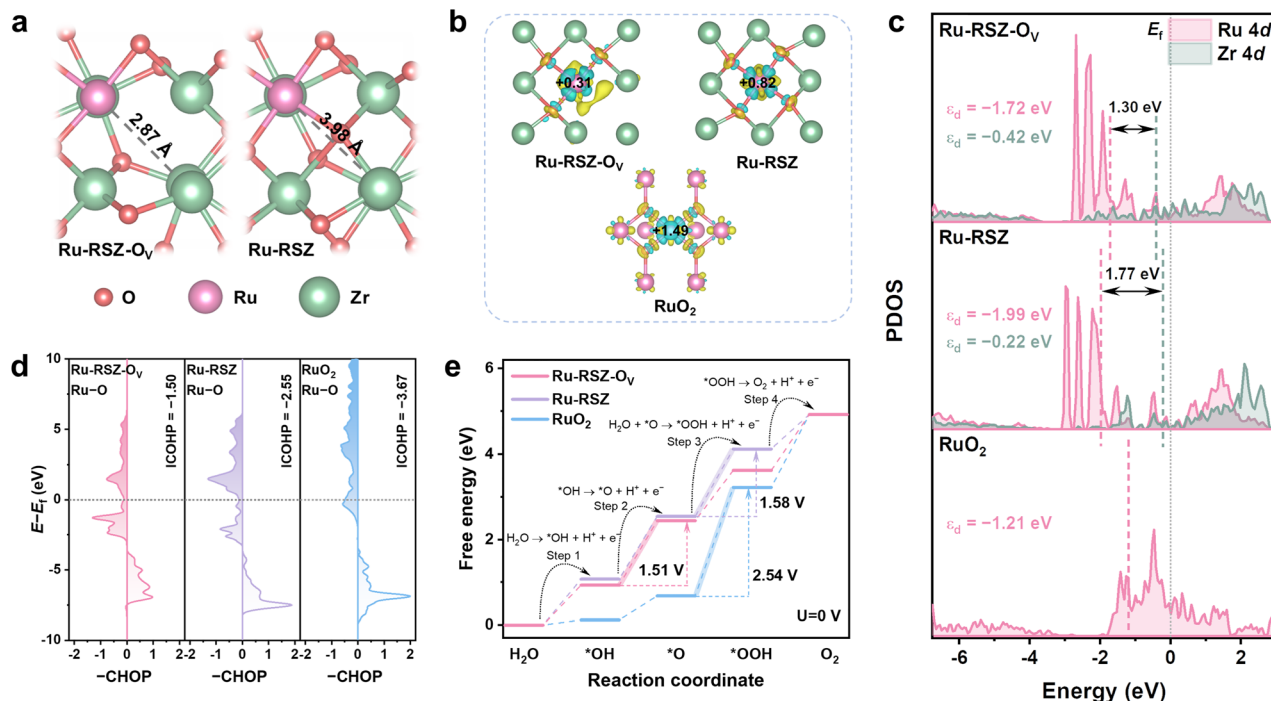


Fig. 4 Theoretical simulation and analysis. (a) Comparison of Ru–Zr atomic distances in Ru–RSZ–O<sub>v</sub> (left) and Ru–RSZ (right). (b) Differential charge density and Bader charge calculation of Ru–RSZ–O<sub>v</sub>, Ru–RSZ and RuO<sub>2</sub> (yellow indicates charge accumulation, while blue indicates charge depletion). (c) The PDOS of Ru 4d and Zr 4d for Ru–RSZ–O<sub>v</sub>, Ru–RSZ and RuO<sub>2</sub>. (d) Calculated COHP of Ru–RSZ–O<sub>v</sub>, Ru–RSZ and RuO<sub>2</sub>. (e) Gibbs free energy diagrams via the AEM pathway on the Ru site at U = 0 V for Ru–RSZ–O<sub>v</sub>, Ru–RSZ and RuO<sub>2</sub>.

(+1.2822|e|), providing clear evidence for electron transfer from Zr to Ru, aligning with the valence state trend measured by XAS, jointly confirming the metal–support electronic synergy.

In-depth analysis of the electronic structure shows that the PDOS (Fig. 4c) of the Ru-4d and Zr-4d orbitals in Ru-RSZ-O<sub>v</sub> exhibits significantly enhanced peak overlap and hybridization near the Fermi level, confirming the effective promotion of d–d orbital coupling between Ru and Zr by the oxygen vacancies.<sup>48</sup> Furthermore, the separation between their d-band centers contracts from 1.77 eV in Ru-RSZ to 1.30 eV in Ru-RSZ-O<sub>v</sub>, implying a reduced average energy difference and closer spatial distribution between the Ru-4d and Zr-4d orbitals, which further supports the conclusion of enhanced d–d orbital coupling. This coupling drives electron transfer from Zr to Ru, resulting in a moderate upshift of the Ru d-band center (from -1.99 eV to -1.72 eV) and a concomitant downshift of the Zr d-band center (from -0.42 eV to -0.22 eV) in Ru-RSZ-O<sub>v</sub>, a theoretically calculated charge redistribution that is consistent with the XAS analysis. The moderate upshift of the Ru d-band center facilitates the optimization of its adsorption free energy for OER intermediates, thereby enhancing the intrinsic activity.<sup>49</sup> Concurrently, its energy level remains substantially lower than that of RuO<sub>2</sub> (-1.21 eV), which is beneficial for suppressing the over-oxidation of Ru and consequently improving the electrochemical stability.

Direct evidence for chemical bond strengthening is provided by ICOHP analysis. The ICOHP value for the Ru–Zr atomic pair (Fig. S21) decreases significantly from -0.001 eV in Ru-RSZ to

-0.089 eV in Ru-RSZ-O<sub>v</sub>, demonstrating a significant enhancement of the Ru–Zr bond induced by the oxygen vacancies. Simultaneously, analysis of the Ru site reveals that the ICOHP value (Fig. 5d) for the Ru–O bond in Ru-RSZ-O<sub>v</sub> exhibits a less negative value (-1.50 eV) compared to those in Ru-RSZ (-2.55 eV) and RuO<sub>2</sub> (-3.067 eV), indicating a weakened covalent character. This attenuation is attributed to the Ru–Zr d–d orbital coupling, which effectively modulates the adsorption strength of oxygenated intermediates on the Ru active sites, thereby optimizing the reaction kinetics of the OER. Furthermore, pH-dependent and tetramethylammonium cation (TMA<sup>+</sup>) probing measurements were further used to demonstrate the restricted lattice oxygen activity in Ru-RSZ (Fig. S22–24). According to the calculated proton reaction orders ( $\rho = \partial \log(j) / \partial \text{pH}$ ), RuO<sub>2</sub> shows significant pH-dependent ( $\rho = -0.165$ ) OER activity, whereas Ru-RSZ reflects a pH-independent ( $\rho = -0.076$ ) characteristic in which the current density nearly remains constant as the pH value changes. This result indicates that the degree of non-equilibrium proton–electron coupling transfer of Ru-RSZ has decreased.<sup>23</sup> Moreover, the addition of TMA<sup>+</sup> in 0.5 M H<sub>2</sub>SO<sub>4</sub> does not affect the OER activity of Ru-RSZ, whereas a clear inhibition is observed for RuO<sub>2</sub>, indicating that the amount of \*OO intermediates produced by Ru-RSZ is lower, demonstrating that the extent of lattice oxygen involvement in the OER process is reduced and the stability of the lattice structure has been optimized.<sup>50</sup> Gibbs free energy calculations (Fig. 5e, S25 and S26) demonstrate that the adsorption energies of Ru-RSZ-O<sub>v</sub> for all OER intermediates lie between those of Ru-



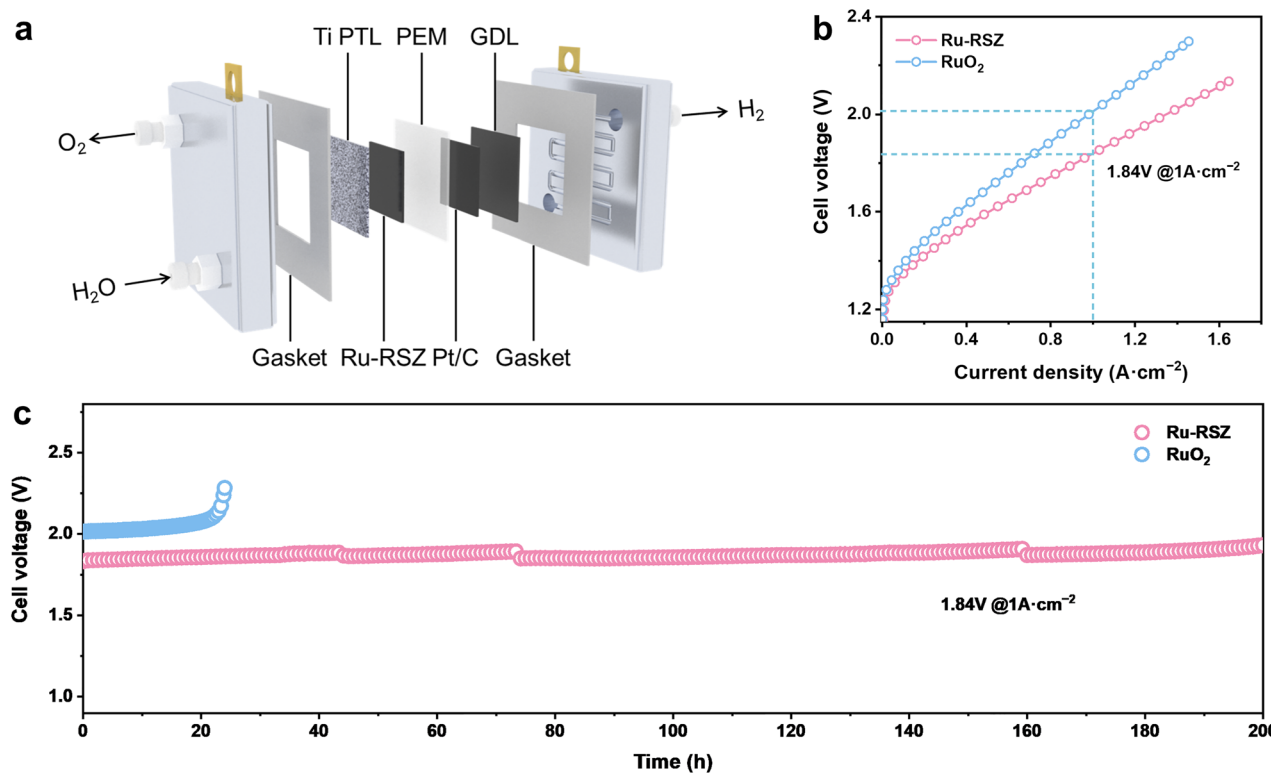


Fig. 5 (a) Schematic diagram of the PEM electrolyzer using Ru-RSZ as the anode electrocatalyst. (b) Polarization curves of PEMWE employing Ru-RSZ and RuO<sub>2</sub> as the anodic electrocatalyst. (c) Chronopotentiometry curve of Ru-RSZ and RuO<sub>2</sub> in a PEMWE electrolyzer at 1 A cm<sup>-2</sup>.

RSZ and RuO<sub>2</sub>, achieving a more balanced adsorption strength.<sup>51</sup> Concurrently, the rate-determining step (RDS) energy barrier for Ru-RSZ-O<sub>v</sub> is the lowest (1.51 eV, \*OH → \*O + H<sup>+</sup> + e<sup>-</sup>) among the studied catalysts, being lower than those for Ru-RSZ (1.58 eV, H<sub>2</sub>O + \*O → \*OOH + H<sup>+</sup> + e<sup>-</sup>) and RuO<sub>2</sub> (2.41 eV). The change in the RDS coupled with the significant reduction in the energy barrier collectively contributes to the enhanced OER activity.<sup>30</sup> The vacancy formation energy calculations (Fig. S27) indicate that the Ru vacancy formation energy in Ru-RSZ-O<sub>v</sub> (8.94 eV) is higher than those in RuO<sub>2</sub> (8.22 eV) and Ru-RSZ (8.68 eV), suggesting greater resistance of the Ru species to dissolution, which further corroborates, from a thermodynamic perspective, the crucial role of d-d orbital coupling in enhancing OER stability.

### PEMWE performance evaluation

To further verify the performance of Ru-RSZ for practical applications in water electrolysis, a membrane electrode assembly was constructed utilizing a Nafion 211 membrane with Ru-RSZ as the anode catalyst and commercial Pt/C as the cathode catalyst, respectively (Fig. 5a). The mass loading of Ru in the anode of the PEMWE tests is 175.7 μg<sub>Ru</sub> cm<sup>-2</sup>. The polarization curve (without *iR* compensation) confirms the superior catalytic activity of Ru-RSZ compared to commercial RuO<sub>2</sub>. Specifically, the Ru-RSZ-based PEMWE electrolyzer delivers a current density of 1 A cm<sup>-2</sup> at a cell voltage of 1.84 V, which is 180 mV lower than the voltage required by commercial

RuO<sub>2</sub> (Fig. 5b).<sup>11,52</sup> Furthermore, the long-term stability of the PEMWE with the Ru-RSZ anode was evaluated by the CP test at a constant current density of 1 A cm<sup>-2</sup> (Fig. 5c). The result indicates that the cell voltage remained stable throughout the 200-hour test period, with no significant increase observed. These results strongly confirm that the electronic regulation of Ru by the ZrO<sub>2</sub> support could enhance both the catalytic activity and stability of Ru-RSZ, demonstrating significant potential for practical application in PEMWE.

## Conclusions

In summary, this work reports the synthesis of a Ru electrocatalyst anchored on a zirconia support (Ru-RSZ), wherein the electronic structure of the Ru active sites is precisely modulated through the establishment of Ru-Zr 4d-4d coupling *via* oxygen vacancy generation, leading to substantially improved activity and stability for acidic OER. The successful stabilization of the tetragonal ZrO<sub>2</sub> phase upon Ru incorporation was confirmed by XRD and Raman spectroscopy, while the formation of oxygen vacancies induced by Ru doping was evidenced by XAS and XPS analyses. DFT calculations provide a mechanistic foundation, showing that the coupling redistributes electron density and weakens the binding strength of oxygen intermediates, thereby optimizing the reaction kinetics. The optimized Ru-RSZ electrode delivers a low overpotential of 208 mV at 10 mA cm<sup>-2</sup> and a mass activity (1452.61 A g<sub>Ru</sub><sup>-1</sup> @ 1.51 V) 40.1 times greater than that of commercial RuO<sub>2</sub>. Its practical viability is further



demonstrated in a PEMWE cell, achieving 1.84 V at 1 A cm<sup>-2</sup> with stable operation for >200 h. Consequently, this work presents a rational and effective strategy for the development of efficient and durable Ru-based electrocatalysts for practical renewable energy conversion technologies.

## Author contributions

D. Yu conceived the project, performed all the electrochemical measurements, and wrote the initial draft of the manuscript. H. Zhao and Y. Zhang reviewed and edited the manuscript. B. Liu, D. Li, and J. Yu provided useful discussions and insights. X. Li and S. Liu contributed to the interpretation of the experimental results. Z. Li and P. Gao supervised the research. All authors contributed to the manuscript.

## Conflicts of interest

The authors declare no competing financial interest.

## Data availability

The data supporting the findings of this article are available within the paper and the supplementary information (SI). Supplementary information is available. See DOI: <https://doi.org/10.1039/d6sc01575a>.

## Acknowledgements

This work was financially supported by the National Natural Science Foundation of China (22478450), the Sichuan Province Science and Technology Education Joint Fund Project (2025NSFSC2057), the Liaoning Binhai Laboratory Project (LBLEF-202306) and the Science and Technology Foundation of Dalian City (2022JJ11CG005).

## Notes and references

- H. Jun, E. Kang, J. Moon, H. Kim, S. Han, S. Choung, S. Kim, S. Y. Yi, E. Kang, C. H. Choi, J. W. Han and J. Lee, *Chem*, 2025, **11**, 102367.
- Y. Jiao, Y. Zheng, M. Jaroniec and S. Z. Qiao, *Chem. Soc. Rev.*, 2015, **44**, 2060–2086.
- X. Wang, Z. Li, H. Jang, C. Chen, S. Liu, L. Wang, M. G. Kim, J. Cho, Q. Qin and X. Liu, *Adv. Energy Mater.*, 2024, **15**, 2403388.
- S. Yang, Q. Shu, B. Fu, S. Liu, Y. Zhang and H. Zhao, *Chem. Eng. J.*, 2024, **488**, 150905.
- R.-T. Liu, Z.-L. Xu, F.-M. Li, F.-Y. Chen, J.-Y. Yu, Y. Yan, Y. Chen and B. Y. Xia, *Chem. Soc. Rev.*, 2023, **52**, 5652–5683.
- C.-Z. Yuan, S. Wang, K. San Hui, K. Wang, J. Li, H. Gao, C. Zha, X. Zhang, D. A. Dinh, X.-L. Wu, Z. Tang, J. Wan, Z. Shao and K. N. Hui, *ACS Catal.*, 2023, **13**, 2462–2471.
- R. Ram, L. Xia, H. Benzidi, A. Guha, V. Golovanova, A. Garzon Manjon, D. Llorens Rauret, P. Sanz Berman, M. Dimitropoulos, B. Mundet, E. Pastor, V. Celorrio, C. A. Mesa, A. M. Das, A. Pinilla-Sanchez, S. Gimenez, J. Arbiol, N. Lopez and F. P. Garcia de Arquer, *Science*, 2024, **384**, 1373–1380.
- Z.-P. Wu, H. Zhang, S. Zuo, Y. Wang, S. L. Zhang, J. Zhang, S.-Q. Zang and X. W. Lou, *Adv. Mater.*, 2021, **33**, 2103004.
- J. Chen, J. Ma, T. Huang, Q. Liu, X. Liu, R. Luo, J. Xu, X. Wang, T. Jiang, H. Liu, Z. Lv, T. Yao, G. Wang, X. Zheng, Z. Li and W. Chen, *Angew. Chem., Int. Ed.*, 2025, **64**, e202503330.
- J. Park, D. W. Lee, J. Hyun, H. Lee, E. Oh, K. Seok, G. Doo and H.-T. Kim, *Energy Environ. Sci.*, 2025, **18**, 5577–5585.
- W. He, X. Tan, Y. Guo, Y. Xiao, H. Cui and C. Wang, *Angew. Chem., Int. Ed. Engl.*, 2024, **63**, e202405798.
- M. Zhang, W. An, Q. Liu, Y. Jiang, X. Zhao, H. Chen, Y. Zou, X. Liang and X. Zou, *Nat. Commun.*, 2025, **16**, 7608.
- J. Chen, Y. Ma, T. Huang, T. Jiang, S. Park, J. Xu, X. Wang, Q. Peng, S. Liu, G. Wang and W. Chen, *Adv. Mater.*, 2024, **36**, e2312369.
- G. Chen, R. Lu, C. Ma, X. Zhang, Z. Wang, Y. Xiong and Y. Han, *Angew. Chem., Int. Ed. Engl.*, 2024, **63**, e202411603.
- L. Li, G. Zhang, C. Zhou, F. Lv, Y. Tan, Y. Han, H. Luo, D. Wang, Y. Liu, C. Shang, L. Zeng, Q. Huang, R. Zeng, N. Ye, M. Luo and S. Guo, *Nat. Commun.*, 2024, **15**, 4974.
- Y. Shen, X.-L. Zhang, M.-R. Qu, J. Ma, S. Zhu, Y.-L. Min, M.-R. Gao and S.-H. Yu, *Nat. Commun.*, 2024, **15**, 7861.
- J. Chen, Y. Ma, C. Cheng, T. Huang, R. Luo, J. Xu, X. Wang, T. Jiang, H. Liu, S. Liu, T. Huang, L. Zhang and W. Chen, *J. Am. Chem. Soc.*, 2025, **147**, 8720–8731.
- J. Zhang, H. Qin, X. Cao, W. Jia, R. Ma, X. Chen, W. Xia, G. Lin and L. Jiao, *ACS Mater. Lett.*, 2024, **6**, 3016–3024.
- Y. Qin, S. Deng, X.-Y. Zhou, Z. Yan, L. He, K. Li and T.-Y. Zhang, *J. Am. Chem. Soc.*, 2025, **147**, 30943–30955.
- L. Deng, H. Chen, S.-F. Hung, Y. Zhang, H. Yu, H.-Y. Chen, L. Li and S. Peng, *J. Am. Chem. Soc.*, 2024, **146**, 35438–35448.
- X. Li, H. Rong, J. Zhang, D. Wang and Y. Li, *Nano Res.*, 2020, **13**, 1842–1855.
- C. Zhou, L. Li, Z. Dong, F. Lv, H. Guo, K. Wang, M. Li, Z. Qian, N. Ye, Z. Lin, M. Luo and S. Guo, *Nat. Commun.*, 2024, **15**, 9774.
- X. Zhang, Y. Zhang, B. O. Protsenko, M. A. Soldatov, J. Zhang, C. Yang, S. Bo, H. Wang, X. Chen, C. Wang, W. Cheng and Q. Liu, *Nat. Commun.*, 2025, **16**, 6921.
- Y. Li, J. Zhao, S. Zhang, Y. Fan, C. Y. Kuo, Y. C. Ku, T. S. Chan, C. W. Kao, Y. C. Huang, C. T. Chen, S. C. Haw, C. Jin, H. Zhao, D. Ye, C. Jing, Z. Hu and L. Zhang, *J. Am. Chem. Soc.*, 2025, **147**, 26854–26864.
- B.-J. Kim, D. F. Abbott, X. Cheng, E. Fabbri, M. Nachtegaal, F. Bozza, I. E. Castelli, D. Lebedev, R. Schäublin, C. Copéret, T. Graule, N. Marzari and T. J. Schmidt, *ACS Catal.*, 2017, **7**, 3245–3256.
- Z.-Q. Jiang, C.-Z. Fan, J.-Y. Pan, L. Shao, H. Chen, E. Pervaiz, Y. Dong, T.-Z. Wang, X.-R. Zheng, J.-H. Li and Y.-D. Deng, *Rare Met.*, 2024, **43**, 2891–2912.
- H. Yu, C. Wang, X. Xin, Y. Wei, S. Li, Y. An, F. Sun, T. Lin and L. Zhong, *Nat. Commun.*, 2024, **15**, 5143.
- Y. Lin, Z. Tian, L. Zhang, J. Ma, Z. Jiang, B. J. Deibert, R. Ge and L. Chen, *Nat. Commun.*, 2019, **10**, 162.



- 29 F. Wang, L. Feng, M. Zhang and H. Cong, *Nat. Commun.*, 2025, **16**, 6624.
- 30 J. Zhang, L. Xu, X. Yang, S. Guo, Y. Zhang, Y. Zhao, G. Wu and G. Li, *Angew. Chem., Int. Ed.*, 2024, **63**, e202405641.
- 31 T. Wu, X. Zhu, Z. Xing, S. Mou, C. Li, Y. Qiao, Q. Liu, Y. Luo, X. Shi, Y. Zhang and X. Sun, *Angew. Chem., Int. Ed. Engl.*, 2019, **58**, 18449–18453.
- 32 W. Q. Zaman, W. Sun, M. Tariq, Z. Zhou, U. Farooq, Z. Abbas, L. Cao and J. Yang, *Appl. Catal., B*, 2019, **244**, 295–302.
- 33 M. C. Uribe López, M. A. Alvarez Lemus, M. C. Hidalgo, R. López González, P. Quintana Owen, S. Oros-Ruiz, S. A. Uribe López and J. Acosta, *J. Nanomater.*, 2019, **2019**, 1–12.
- 34 C. Li, Z. Han, Y. Hu, T. Liu and X. Pan, *RSC Adv.*, 2022, **12**, 27309–27320.
- 35 C. Dong, R. Mu, R. Li, J. Wang, T. Song, Z. Qu, Q. Fu and X. Bao, *J. Am. Chem. Soc.*, 2023, **145**, 17056–17065.
- 36 Z. Zhang, S. Lu, M. Zhu, F. Wang, K. Yang, B. Dong, Q. Yao and W. Hu, *J. Am. Chem. Soc.*, 2025, **147**, 22806–22817.
- 37 N. Zhang, Y. Hu, L. An, Q. Li, J. Yin, J. Li, R. Yang, M. Lu, S. Zhang, P. Xi and C. H. Yan, *Angew. Chem., Int. Ed. Engl.*, 2022, **61**, e202207217.
- 38 X. Fang, S. Wu, Y. Wu, W. Yang, Y. Li, J. He, P. Hong, M. Nie, C. Xie, Z. Wu, K. Zhang, L. Kong and J. Liu, *Appl. Surf. Sci.*, 2020, **518**, 146226.
- 39 M. Yang, X. Guan, Z. Shi, H. Wu, Y. Cheng, Z. Wang, W. Liu, F. Xiao, M. Shao, M. Xiao, C. Liu and W. Xing, *Small*, 2025, **22**, 2411117.
- 40 Z. Li, H. Sheng, Y. Lin, H. Hu, H. Sun, Y. Dong, X. Chen, L. Wei, Z. Tian, Q. Chen, J. Su and L. Chen, *Adv. Funct. Mater.*, 2024, **34**, 2409714.
- 41 J. Zhao, Y. Guo, Z. Zhang, X. Zhang, Q. Ji, H. Zhang, Z. Song, D. Liu, J. Zeng, C. Chuang, E. Zhang, Y. Wang, G. Hu, M. A. Mushtaq, W. Raza, X. Cai and F. Ciucci, *Nat. Nanotechnol.*, 2025, **20**, 57–66.
- 42 R. Deng, F. Liu, S. Gao, Z. Xia, R. Wu, J. Kong, J. Yang, J. Wen, X. Zhang, C. Lv, Y. Wang, X. Li and Z. Wang, *ACS Catal.*, 2025, **15**, 1782–1794.
- 43 Q. Yao, J. Le, S. Yang, J. Cheng, Q. Shao and X. Huang, *Chin. J. Catal.*, 2022, **43**, 1493–1501.
- 44 J. M. P. Martirez and E. A. Carter, *J. Am. Chem. Soc.*, 2019, **141**, 693–705.
- 45 S. Wang, Q. Jiang, S. Ju, C. S. Hsu, H. M. Chen, D. Zhang and F. Song, *Nat. Commun.*, 2022, **13**, 6650.
- 46 Q. Ji, B. Tang, X. Zhang, C. Wang, H. Tan, J. Zhao, R. Liu, M. Sun, H. Liu, C. Jiang, J. Zeng, X. Cai and W. Yan, *Nat. Commun.*, 2024, **15**, 8089.
- 47 Q. Qin, Z. Li, X. Zhao, H. Zhao, L. Zhai, M. Gyu Kim, J. Cho, H. Jang, S. Liu and X. Liu, *Angew. Chem., Int. Ed. Engl.*, 2025, **64**, e202413657.
- 48 H. Wang, T. Zhai, Y. Wu, T. Zhou, B. Zhou, C. Shang and Z. Guo, *Adv. Sci.*, 2023, **10**, 2301706.
- 49 Y. Qin, T. Yu, S. Deng, X.-Y. Zhou, D. Lin, Q. Zhang, Z. Jin, D. Zhang, Y.-B. He, H.-J. Qiu, L. He, F. Kang, K. Li and T.-Y. Zhang, *Nat. Commun.*, 2022, **13**, 3784.
- 50 K. Zhou, Y. Wang, Z. Jiang, B. Dai and Z. J. Jiang, *Adv. Mater.*, 2025, **37**, 2420159.
- 51 Y. Xu, Z. Mao, J. Zhang, J. Ji, Y. Zou, M. Dong, B. Fu, M. Hu, K. Zhang, Z. Chen, S. Chen, H. Yin, P. Liu and H. Zhao, *Angew. Chem., Int. Ed.*, 2024, **63**, e202316029.
- 52 Z.-Y. Wu, F.-Y. Chen, B. Li, S.-W. Yu, Y. Z. Finfrook, D. M. Meira, Q.-Q. Yan, P. Zhu, M.-X. Chen, T.-W. Song, Z. Yin, H.-W. Liang, S. Zhang, G. Wang and H. Wang, *Nat. Mater.*, 2023, **22**, 100–108.

